

Elastic and transport properties of topological semimetal ZrTe

San-Dong Guo, Yue-Hua Wang and Wan-Li Lu

School of Physics, China University of Mining and Technology, Xuzhou 221116, Jiangsu, China

Topological semimetal may have substantial applications in electronics, spintronics and quantum computation. Recently, ZrTe is predicted as a new type of topological semimetal due to coexistence of Weyl fermion and massless triply degenerate nodal points. In this work, the elastic and transport properties of ZrTe are investigated by combining the first-principles calculations and semiclassical Boltzmann transport theory. Calculated elastic constants prove mechanical stability of ZrTe, and the bulk modulus, shear modulus, Young's modulus and Poisson's ratio also are calculated. It is found that spin-orbit coupling (SOC) has slightly enhanced effects on Seebeck coefficient, which along a(b) and c directions for pristine ZrTe at 300 K is $46.26 \mu\text{V/K}$ and $80.20 \mu\text{V/K}$, respectively. By comparing the experimental electrical conductivity of ZrTe (300 K) with calculated value, the scattering time is determined for 1.59×10^{-14} s. The predicted room-temperature electronic thermal conductivity along a(b) and c directions is $2.37 \text{ Wm}^{-1}\text{K}^{-1}$ and $2.90 \text{ Wm}^{-1}\text{K}^{-1}$, respectively. The room-temperature lattice thermal conductivity is predicted as $17.56 \text{ Wm}^{-1}\text{K}^{-1}$ and $43.08 \text{ Wm}^{-1}\text{K}^{-1}$ along a(b) and c directions, showing very strong anisotropy. Calculated results show that isotope scattering produces observable effect on lattice thermal conductivity. To observably reduce lattice thermal conductivity by nanostructures, the characteristic length should be smaller than 70 nm, based on cumulative lattice thermal conductivity with respect to phonon mean free path(MFP) at 300 K. It is noted that average room-temperature lattice thermal conductivity of ZrTe is slightly higher than that of isostructural MoP, which is due to larger phonon lifetimes and smaller Grüneisen parameters. Finally, the total thermal conductivity as a function of temperature is predicted for pristine ZrTe. Our works provide valuable informations for ZrTe-based nano-electronics devices, and motivate further experimental works to study elastic and transport properties of ZrTe.

PACS numbers: 72.15.Jf, 71.20.-b, 71.70.Ej, 79.10.-n

Email: guosd@cumt.edu.cn

Keywords: Elastic constants; Seebeck coefficient; Lattice thermal conductivity; Topological semimetal

I. INTRODUCTION

From topological insulator to semimetal, the recent discovery of new type of topological nontrivial phase has sparked intense research interest in condensed matter physics and material science¹⁻¹¹. The representative topological semimetals include Dirac semimetals, Weyl semimetals and nodal line semimetals^{3,7,10}, such as Na₃Bi as a classic Dirac Semimetal⁷, TaAs as a representative Weyl semimetal⁸ and ZrSiS as a typical nodal line semimetal⁹, which have been confirmed by angle-resolved photoemission spectroscopy (ARPES). In Dirac and Weyl semimetals, four-fold degenerate Dirac point and two-fold degenerate Weyl point can be observed in the momentum space^{7,8,10,11}, while two bands cross in the form of a periodically continuous line or closed ring for node-line semimetals^{3,9}.

Beyond Dirac and Weyl fermions, some new types of topological semimetals are proposed, which are identified by three-, six- or eight-fold band crossings¹². By the crossing of a double-degeneracy band and a non-degeneracy band, the three-fold degenerate crossing points are predicted in the materials with WC-type structure, such as MoP, WC and ZrTe^{13,14}, and in InAs_{0.5}Sb_{0.5}¹⁵. Then, the ARPES declares the presence of a triply degenerate point in MoP, and pairs of Weyl points coexist with the three-component fermions². Experimentally, the highly metallic characteristics with remarkably low resistivity and high mobility (2 K) has been found in MoP¹⁶. The recent ARPES experiments and

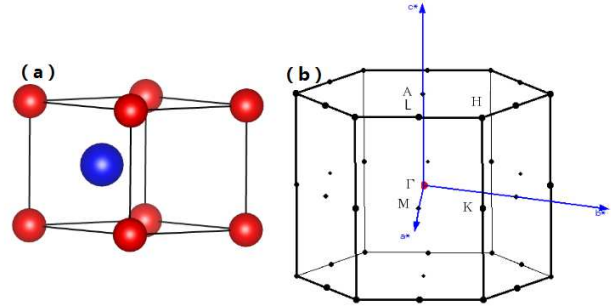


FIG. 1. (Color online) (a)The crystal structure of ZrTe in one unit cell, and the blue and red balls represent Zr and Te atoms. (b)the Brillouin zone with high-symmetry points.

transport measurements have also shown that WC has the nontrivial topological nature^{17,18}. The experimental results of the magnetoresistance, Hall effect, and quantum Shubnikov-de Haas oscillations on single crystals of ZrTe have been reported, indicating ZrTe with low carrier density, high carrier mobility, small cross-sectional area of Fermi surface, and light cyclotron effective mass¹⁹.

Recently, the elastic and thermal transport properties of some representative topological semimetals have been investigated, such TaAs and MoP²⁰⁻²³. The lattice thermal conductivity of both TaAs and MoP shows obvious anisotropy along the a(b) and c crystal axis^{20,21,23}. High thermoelectric performance of TaAs has been predicted, and the maximum thermoelectric figure of merit ZT is up

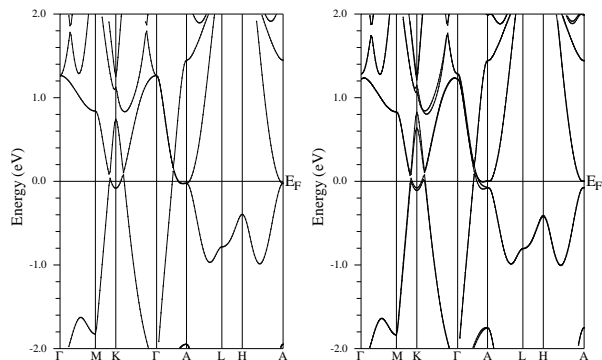


FIG. 2. The calculated energy band structures of ZrTe along high-symmetry paths with GGA (Left) and GGA+SOC (Right).

to 0.63 (900 K) in n-type doping along c direction²¹. In this work, the elastic and transport properties of three-fold degeneracy topological semimetal ZrTe are investigated by combining the first-principles calculations and semiclassical Boltzmann transport theory. The elastic constants, bulk modulus, shear modulus, Young's modulus and Poisson's ratio are predicted with the generalized gradient approximation (GGA). The electronic transport coefficients are also calculated using both GGA and GGA+SOC. It is found that SOC has slight influences on electronic transport coefficients. For pristine ZrTe, the Seebeck coefficient, electrical conductivity, power factor and electronic thermal conductivity are calculated, which can be verified by future experiments. The lattice thermal conductivity as a function of temperature is predicted within GGA, which shows a distinct anisotropic property along the $a(b)$ and c crystal axis. Similar results can be found in topological semimetals TaAs and MoP^{20,21,23}. The isotope and size effects on the lattice thermal conductivity are also studied, and the phonon mode analysis is also performed to understand deeply phonon transport of ZrTe. The total lattice thermal conductivity ($\kappa = \kappa_L + \kappa_e$) as a function of temperature is also predicted for pristine ZrTe. This work sheds light on the elastic and transport properties of ZrTe, and could offer valuable guidance for MoP-based nano-electronics devices.

The rest of the paper is organized as follows. In the next section, we shall give our computational details. In the third section, we shall present elastic and transport properties of ZrTe. Finally, we shall give our conclusions in the fourth section.

II. COMPUTATIONAL DETAIL

Within the density functional theory (DFT)²⁴, a full-potential linearized augmented-plane-waves method, using GGA of Perdew, Burke and Ernzerhof (GGA-PBE)³⁴, is employed to investigate electronic structures of ZrTe, as implemented in the WIEN2k code²⁶. The

SOC is included self-consistently²⁷⁻³⁰, which produces observable effects on electronic transport coefficients. The convergence results are determined by using 4000 k-points in the first Brillouin zone (BZ) for the self-consistent calculation, making harmonic expansion up to $l_{\max} = 10$ in each of the atomic spheres, and setting $R_{\text{mt}} * k_{\max} = 8$ for the plane-wave cut-off. The self-consistent calculations are considered to be converged when the integration of the absolute charge-density difference between the input and output electron density is less than $0.0001|e|$ per formula unit, where e is the electron charge. Based on calculated energy band structures, transport coefficients of electron part are calculated through solving Boltzmann transport equations within the constant scattering time approximation (CSTA), as implemented in BoltzTrap code³¹. To obtain accurate transport coefficients, the parameter LPFAC is set as 10, and 2772 k-points is used in the irreducible BZ for the calculations of energy band structures.

TABLE I. The experimental lattice constants a and c (Å); elastic constants C_{ij} , bulk (B), shear (G) and Young's (E_{xx} and E_{zz}) moduli (in GPa); Poisson's ratio (ν).

a	c	C_{11}	C_{12}	C_{13}	C_{33}	C_{44}
3.771	3.861	140.82	58.78	88.81	201.11	110.36
B	G	E_{xx}	E_{zz}	$\nu_{xy/yx}$	$\nu_{xz/yz}$	$\nu_{zx/zy}$
102.50	61.26	97.83	122.07	0.19	0.36	0.45

For elastic properties and phonon transport, the first-principles calculations are performed within the projected augmented wave (PAW) method, and the GGA-PBE is adopted as exchange-correlation energy functional, as implemented in the VASP code³²⁻³⁵. A plane-wave basis set is employed with kinetic energy cutoff of 400 eV, and the electronic stopping criterion is 10^{-8} eV. The lattice thermal conductivity of ZrTe is performed by solving linearized phonon Boltzmann equation with the single mode relaxation time approximation (RTA), as implemented in the Phono3py code³⁶. The lattice thermal conductivity can be expressed as

$$\kappa_L = \frac{1}{NV_0} \sum_{\lambda} \kappa_{\lambda} = \frac{1}{NV_0} \sum_{\lambda} C_{\lambda} \nu_{\lambda} \otimes \nu_{\lambda} \tau_{\lambda} \quad (1)$$

where λ is phonon mode, N is the total number of q points sampling the BZ, V_0 is the volume of a unit cell, and C_{λ} , ν_{λ} , τ_{λ} is the specific heat, phonon velocity, phonon lifetime. The interatomic force constants (IFCs) are calculated by the finite displacement method. The second-order harmonic IFCs are calculated using a $4 \times 4 \times 4$ supercell containing 128 atoms with k-point meshes of $2 \times 2 \times 2$. Using the harmonic IFCs, phonon dispersion of ZrTe can be attained by Phonopy package³⁷. The group velocity and specific heat can be attained from phonon dispersion which also determines the allowed three-phonon scattering processes. The third-order

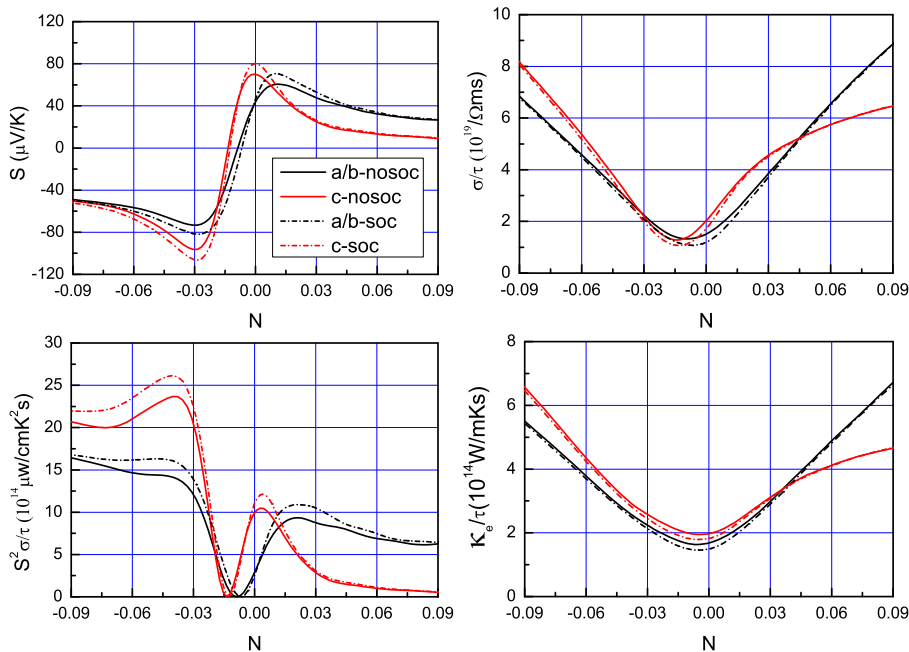


FIG. 3. (Color online) At room temperature (300 K), Seebeck coefficient S , electrical conductivity with respect to scattering time σ/τ , power factor with respect to scattering time $S^2\sigma/\tau$ and electronic thermal conductivity with respect to scattering time κ_e/τ of ZrTe as a function of doping level (N) with GGA and GGA+SOC.

anharmonic IFCs are calculated using a $3 \times 3 \times 3$ supercells containing 54 atoms with k-point meshes of $3 \times 3 \times 3$, and the total number of displacements is 508. Based on third-order anharmonic IFCs, the phonon lifetimes can be attained from the three-phonon scattering. To compute lattice thermal conductivities, the reciprocal spaces of the primitive cells are sampled using the $20 \times 20 \times 20$ meshes.

III. MAIN CALCULATED RESULTS AND ANALYSIS

A. ELASTIC PROPERTIES

The WC-type ZrTe possesses space group $P\bar{6}m2$ (No. 187), with Zr and Te atoms occupying the 1d (1/3, 2/3, 1/2) and 1a (0,0,0) Wyckoff positions, respectively. The crystal structure and BZ of ZrTe are shown in Figure 1. All the results attained in the following are from the calculations with experimental lattice constants ($a=b=3.7707 \text{ \AA}$, $c=3.8606 \text{ \AA}$)³⁸. The most basic physical quantities of elastic properties are elastic constants C_{ij} , which can be used to construct else elastic physical quantities. The elastic constants are a four-rank tensor. However, the elastic constants are reduced to five independent ones: C_{11} , C_{12} , C_{13} , C_{33} , C_{44} due to the symmetry for hexagonal crystal, and C_{66} can be obtained by $(C_{11} - C_{12})/2$. The calculated C_{ij} are shown in Table I. To prove mechanical stability of ZrTe, we use the following mechanical stability criterion for the hexagonal

materials^{39,40}:

$$C_{44} > 0 \quad (2)$$

$$C_{11} > |C_{12}| \quad (3)$$

$$(C_{11} + 2C_{12})C_{33} > 2C_{13}^2 \quad (4)$$

By simple calculations, these criteria are satisfied for ZrTe, which means no strong tendency to become unstable with the increasing pressure.

The Voigt's, Reuss's and Hill's bulk modulus can be attained by the following equations:

$$B_V = \frac{1}{9}(2C_{11} + C_{33} + 2C_{12} + 4C_{13}) \quad (5)$$

$$B_R = (2S_{11} + S_{33} + 2S_{12} + 4S_{13})^{-1} \quad (6)$$

$$B_H = \frac{1}{2}(B_V + B_R) \quad (7)$$

The Voigt's, Reuss's and Hill's shear modulus can be calculated by using these formulas:

$$G_V = \frac{1}{15}(2C_{11} + C_{33} - C_{12} - 2C_{13} + 6C_{44} + 3C_{66}) \quad (8)$$

$$G_R = \left[\frac{1}{15}(8S_{11} + 4S_{33} - 4S_{12} - 8S_{13} + 6S_{44} + 3S_{66}) \right]^{-1} \quad (9)$$

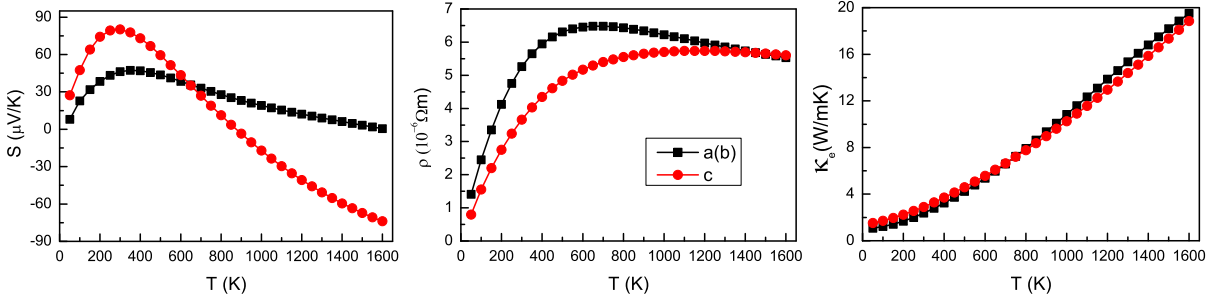


FIG. 4. (Color online) For pristine ZrTe, the Seebeck coefficient S , electrical resistivity ρ and electronic thermal conductivity κ_e as a function of temperature with GGA+SOC.

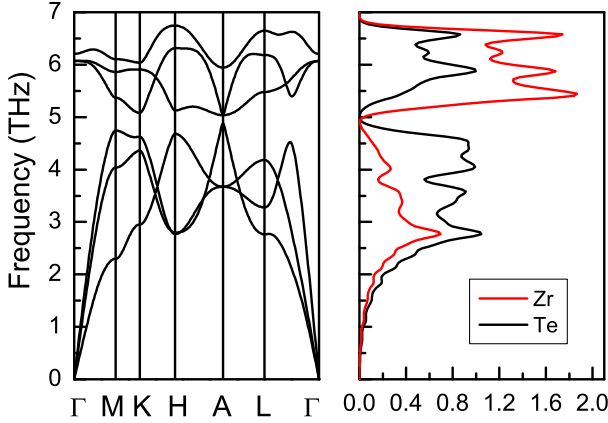


FIG. 5. (Color online) Phonon dispersions of ZrTe with the corresponding atom partial DOS (PDOS).

$$G_H = \frac{1}{2}(G_V + G_R) \quad (10)$$

The S_{ij} 's can be obtained by inverting the elastic constants matrix. The calculated Voigt's, Reuss's and Hill's bulk modulus are 106.17 GPa, 98.82 GPa and 102.50 GPa, respectively, and 68.77 GPa, 53.75 GPa and 61.26 GPa for shear modulus. The Hill's bulk and shear modulus are listed in Table I. The B and G can be used to measure material behaviour as ductile or brittle. If the B/G ratio value is larger than 1.75, the material behaves as ductile, otherwise, it shows a brittle character. For ZrTe, the calculated B/G ratio value with Hill's bulk and shear modulus is 1.67, indicating that the brittle character is dominant. This is different from MoP, where the ductile character is dominant²³.

The Young's modulus E_{ii} can be calculated by the relationship:

$$E_{ii} = 1/S_{ii} \quad (11)$$

The numerical calculated values are $E_{xx}=E_{yy}=97.83$ GPa and $E_{zz}=122.07$ GPa, respectively. The Poisson's ratios ν_{ij} can be calculated by:

$$\nu_{ij} = -S_{ij}/S_{ii} \quad (12)$$

The calculated results are $\nu_{xy}=\nu_{yx}=0.19$, $\nu_{xz}=\nu_{yz}=0.36$ and $\nu_{zx}=\nu_{zy}=0.45$. The characteristics of chemical bonds can be reflected by the Poisson's ratio. For covalent materials, the ν is low with a typical value of 0.10, while for ionic materials with a high typical value of 0.25⁴¹. Based on ν values of ZrTe, ionic bonding is dominant.

B. ELECTRONIC TRANSPORT

The energy band structures of ZrTe along high-symmetry paths are shown in Figure 2 using both GGA and GGA+SOC. Our calculated results agree well with previous theoretical ones¹³. It is found that the six-fold degenerated nodal point splits into the two triply degenerate nodal points (TDNPs) along the Γ -A direction, when the SOC is included¹³. However, the six pairs of Weyl nodes appear around K point in its first BZ¹³. Based on calculated energy band structures, the electronic transport coefficients of ZrTe can be attained using CSTA Boltzmann theory. Although the calculated electrical conductivity depends on scattering time τ using CSTA, the Seebeck coefficient is independent of scattering time, directly compared with experimental results. At room temperature, the Seebeck coefficient S , electrical conductivity with respect to scattering time σ/τ , power factor with respect to scattering time $S^2\sigma/\tau$ and electronic thermal conductivity with respect to scattering time κ_e/τ along a(b) and c directions as a function of doping level using both GGA and GGA+SOC are plotted in Figure 3. Within the framework of rigid band approach, the n- or p-type doping can be simulated by simply shifting Fermi level into conduction or valence bands, which is effective in low doping level⁴²⁻⁴⁴.

Calculated results show that SOC has a slightly enhanced effect on n- and p-type Seebeck coefficient (absolute value) along both a(b) and c directions in low doping level. It is found that the Seebeck coefficients are relatively strongly anisotropic along a(b) and c directions. The calculated S along a(b) and c directions for pristine ZrTe is 46.26 $\mu\text{V/K}$ and 80.20 $\mu\text{V/K}$, respectively, which can be further verified by the experiment. When the See-

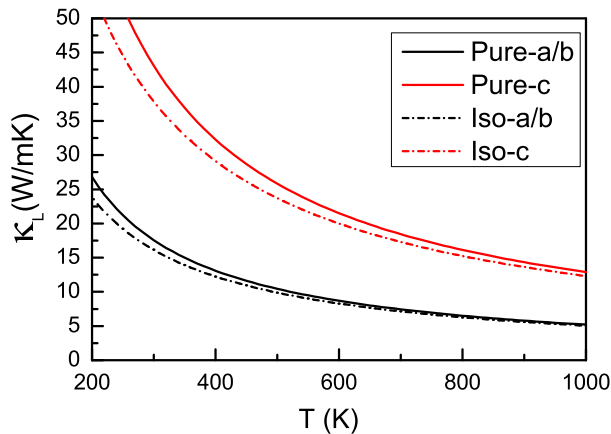


FIG. 6. (Color online) The lattice thermal conductivities of pure and isotopic ZrTe as a function of temperature, including a(b) and c directions.

beck coefficient vanishes, the doping level along a(b) and c directions is about -0.0065 and -0.0124, respectively. It is found that n-type doping has more excellent Seebeck coefficient than p-type doping. For σ/τ , the slightly reduced influence caused by SOC can be observed along both a(b) and c directions. The electronic thermal conductivity κ_e relates to the electrical conductivity σ via the Wiedemann-Franz law:

$$\kappa_e = L\sigma T \quad (13)$$

where L is the Lorenz number. So, there are similar dependencies of doping level and SOC between κ_e/τ and σ/τ . The τ is attained by comparing experimental electrical conductivity¹⁹ of ZrTe with the calculated value of σ/τ at room temperature, and the τ is found to be 1.59×10^{-14} s. For pristine ZrTe, the electronic thermal conductivity along a(b) and c directions is $2.37 \text{ Wm}^{-1}\text{K}^{-1}$ and $2.90 \text{ Wm}^{-1}\text{K}^{-1}$, respectively. Using the calculated τ , the electrical resistivity of pristine ZrTe along a(b) and c directions is $5.26 \times 10^{-6} \text{ } \Omega\text{m}$ and $3.66 \times 10^{-6} \text{ } \Omega\text{m}$, respectively. A enhanced SOC effect on power factor can be observed along both a(b) and c directions, which is due to improved S caused by SOC. For pristine ZrTe, the power factor along a(b) and c directions is $3.82 \text{ } \mu\text{W}/\text{cmK}^2$ and $17.33 \text{ } \mu\text{W}/\text{cmK}^2$, respectively, showing obvious anisotropy.

Next, we obtain the scattering time τ at different temperatures by $\tau \propto T^{-145}$. For pristine ZrTe, the Seebeck coefficient S, electrical resistivity ρ and electronic thermal conductivity κ_e as a function of temperature with GGA+SOC are plotted Figure 4. It is found that the Seebeck coefficient and electrical resistivity along both a(b) and c directions firstly increase with increasing temperature, and then decrease. It is noted that the Seebeck coefficient along c direction changes from positive values to negative ones, when the temperature is larger than 870 K. At high temperature, the electrical resistivity along both a(b) and c directions almost coincides. With in-

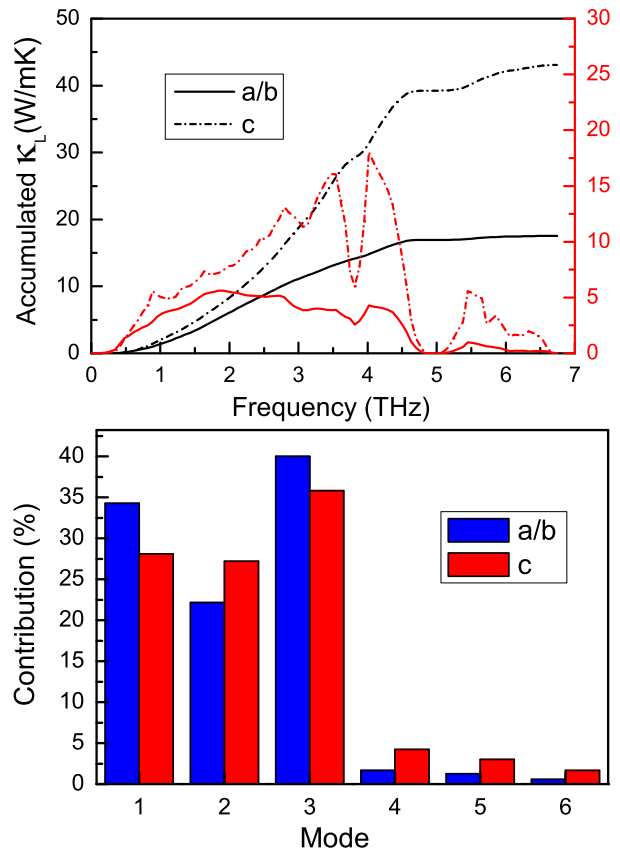


FIG. 7. (Color online) At room temperature (300K), Top: the accumulated lattice thermal conductivities with respect to frequency, and the derivatives. Bottom: the phonon modes contributions along a(b) and c directions toward total lattice thermal conductivity. 1, 2, 3 represent TA1, TA2 and LA branches and 4, 5, 6 for optical branches.

creasing temperature, the electronic thermal conductivity increases along both a(b) and c directions, showing weak anisotropy.

C. PHONON TRANSPORT

Based on the harmonic IFCs, the phonon dispersion of ZrTe can be attained along high-symmetry path, which along with atom partial density of states (DOS) are shown in Figure 5. Due to each primitive cell containing two atoms, there are six vibrational branches consisting of three acoustic and optical ones, respectively. No imaginary frequencies in the phonon dispersion indicate the thermodynamic stability of ZrTe. The ZrTe belongs to $P\bar{6}m2$ space group whose point group is D_{3h} , and then BZ-centre optical phonon modes of this crystal can be decomposed as

$$\Gamma = A_2 + 2E \quad (14)$$

The A_2 and E modes are infrared-active, and E mode is also Raman-active. The phonon frequencies of A_2 and E

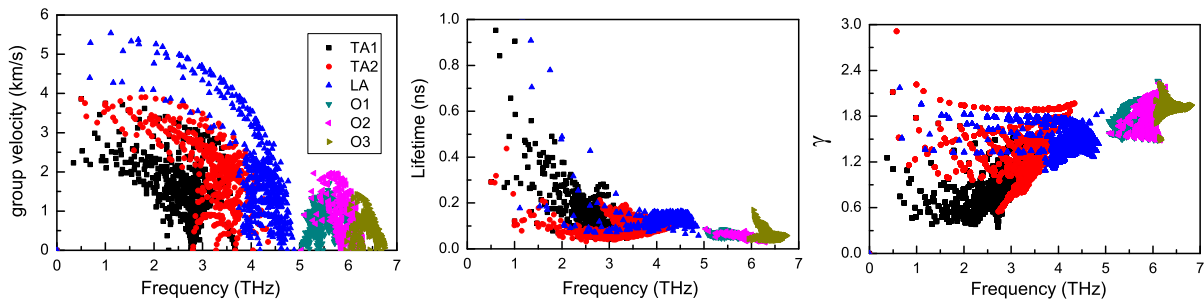


FIG. 8. (Color online) The mode level phonon group velocities, phonon lifetimes (300K) and Grüneisen parameters (γ) of pure ZrTe in the first BZ.

are shown in Table II. It can be clearly seen that there is a well-separated acoustic-optical gap of 0.15 THz at the A point (0, 0, $\pi/2$) on the boundary of the BZ. The top phonon band of the gap at the A point is doubly degenerate, while the bottom phonon band is a singlet state. Similar phonon gap can also be found in MoP²³, which is larger than one of ZrTe. However, the isoelectronic ZrSe shows no acoustic-optical gap, and the presence of the TDNPs of phonon has been predicted⁴⁶. From atom partial DOS, contribution to the acoustic (optical) phonon branches mainly comes from Te (Zr) atoms.

TABLE II. Theoretical optical phonon frequencies (THz) at the Γ point; acoustic-optical gap (THz); lattice thermal conductance (WmK^{-1})

A_2	$E(1)$	$E(2)$	Gap	$\kappa_L(a/b)$	$\kappa_L(c)$
6.21	6.07	6.07	0.15	17.56	43.08

The intrinsic lattice thermal conductivity of ZrTe can be attained from harmonic and anharmonic IFCs by solving the linearized phonon Boltzmann equation within single-mode RTA method. The phonon-isotope scattering is also considered, according to the formula proposed by Shin-ichiro Tamura⁴⁸. The lattice thermal conductivities of pure and isotopic ZrTe along a(b) and c directions as a function of temperature are shown in Figure 6. In the considered temperature region, the intrinsic enhancement of phonon-phonon scattering with increasing temperature leads to the decreased lattice thermal conductivity of ZrTe, which typically results as $1/T$. From Figure 6, it is clearly seen that the lattice thermal conductivity of ZrTe shows obvious anisotropy, where the lattice thermal conductivity along c direction is very higher than that along a(b) direction. Similar result can be found in MoP²³, but is different from TaAs²⁰. At room temperature, the lattice thermal conductivities of pure (isotopic) ZrTe along a(b) and c directions are 17.56 (16.13) $\text{Wm}^{-1}\text{K}^{-1}$ and 43.08 (37.82) $\text{Wm}^{-1}\text{K}^{-1}$, which of pure ZrTe are shown in Table II. To measure the anisotropic strength, an anisotropy factor²⁰ is defined as $\eta = (\kappa_L(cc) - \kappa_L(aa))/\kappa_L(aa)$, and the calculated value is 145.3%, which is larger than that of MoP, im-

plying stronger anisotropy. The lattice thermal conductivity is connected with Young's modulus by the simple relation $\kappa_L \sim \sqrt{E}$ ⁴⁷. Calculated results show that the orders of Young's modulus and lattice thermal conductivity along a(b) and c directions are identical. It is found that phonon-isotope scattering along c direction produces larger effects on lattice thermal conductivity than that along a(b) direction. With increasing temperature, isotopic effect on lattice thermal conductivity gradually decreases, which is due to improvement of phonon-phonon scattering.

At room temperature, the cumulative lattice thermal conductivities with respect to frequency along with the derivatives along a(b) and c directions are plotted in Figure 7. The cumulative thermal conductivity is defined by:

$$\kappa^c(\omega) = \int_0^\omega \Sigma_\lambda \kappa_\lambda \delta(\omega_\lambda - \omega') d\omega' \quad (15)$$

It is clearly seen that the acoustic phonon branches dominate lattice thermal conductivity, up to 96.49% along a(b) direction and 91.12% along c direction. It is found that the optical contribution along c direction is larger than that along a(b) direction. Furthermore, the relative contributions of six phonon branches to the total lattice thermal conductivity along a(b) and c directions at 300K are plotted in Figure 7. Along both a(b) and c directions, longitudinal acoustic (LA) phonon mode has larger contribution than any of two transverse acoustic (TA1 or TA2) phonon modes. It is evident that optical branches along c direction have obvious contribution.

The phonon transport of ZrTe can be further understood with the help of the mode level phonon group velocities and lifetimes, which are plotted in Figure 8. The largest phonon group velocity of TA1, TA2 and LA branches in long-wavelength limit is 2.23 kms^{-1} , 3.86 kms^{-1} and 4.40 kms^{-1} , respectively. In the low frequency region, the most of group velocities of TA2 and TA1 branches are lower than those of LA branch, which leads to main contribution to lattice thermal conductivity from LA branch. It is found that the most of both group velocities and phonon lifetimes of acoustic branches are larger than those of optical branches, which lead to the

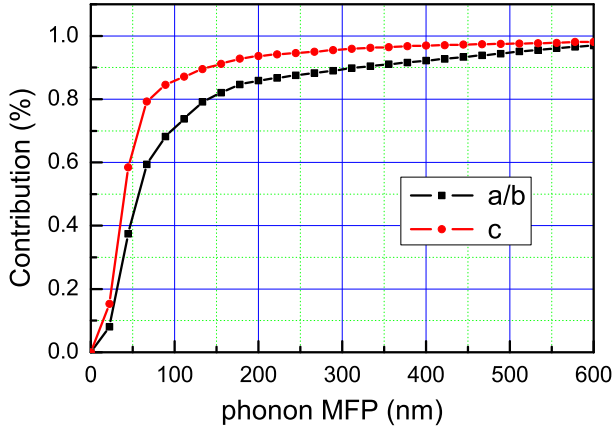


FIG. 9. (Color online) For pure ZrTe, cumulative lattice thermal conductivity divided by total lattice thermal conductivity with respect to phonon MFP along a/b and c directions at room temperature.

dominant contribution from acoustic branches to the total lattice thermal conductivity. The Grüneisen parameters (γ) can reflect the strength of anharmonic interactions, determining the intrinsic phonon-phonon scattering. Here, the Grüneisen parameters are directly calculated by third order anharmonic IFCs. The mode level Grüneisen parameters of pure ZrTe are shown in Figure 8. The larger γ leads to lower phonon lifetimes due to stronger anharmonicity, giving rise to lower lattice thermal conductivity. It is clearly seen that mode phonon lifetimes and Grüneisen parameters show the opposite trend. For all branches, the γ is fully positive. The average Grüneisen parameter is 1.52, indicating relatively strong anharmonic phonon scattering.

To further understand the size dependence of lattice thermal conductivity of ZrTe, the cumulative lattice thermal conductivity divided by total lattice thermal conductivity (CDT) with respect to MFP (300 K) along a(b) and c directions are plotted in Figure 9. The MFP cumulative lattice thermal conductivity is given by:

$$\kappa^c(l) = \int_0^l \sum_{\lambda} \kappa_{\lambda} \delta(l_{\lambda} - l') dl' \quad (16)$$

$$l_{\lambda} = |\lambda| = |\nu_{\lambda} \otimes \tau_{\lambda}| \quad (17)$$

It can reflect the contribution to total lattice thermal conductivity from individual phonon modes with different MFP, namely it shows how phonons with different MFP make contribution to the thermal conductivity. It is clearly seen that the CDT along both a(b) and c directions approaches one with MFP increasing. The contribution from phonons with MFP larger than $0.60 \mu\text{m}$ is very little. Phonons with MFP smaller than 0.13 (0.07) μm along a(b) direction and 0.07 (0.05) μm along c direction contribute around 80% (60%) to the lattice thermal conductivity. It is found that phonons dominating

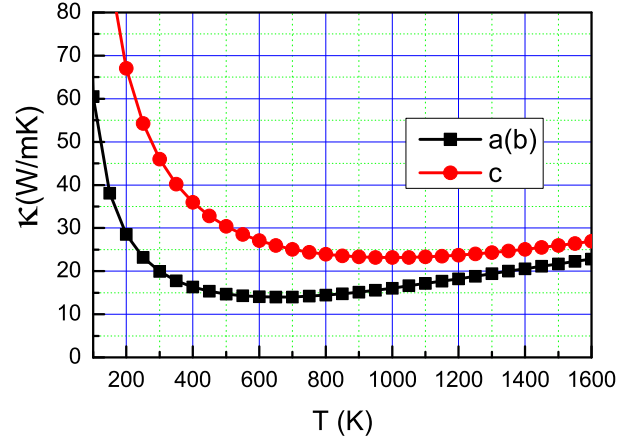


FIG. 10. (Color online) The total thermal conductivities of pristine ZrTe as a function of temperature, including a(b) and c directions.

the lattice thermal conductivity along a(b) direction have longer MFP than ones along c direction.

Based on calculated electronic and lattice thermal conductivity, the total thermal conductivity can be attained, which is plotted in Figure 10. It is clearly seen that κ firstly decreases with increasing temperature, and then increases. It is because lattice part dominates thermal conductivity at low temperature, while electronic part is predominant at high temperature. The minimum κ along a(b) and c directions is $13.98 \text{ Wm}^{-1}\text{K}^{-1}$ and $23.15 \text{ Wm}^{-1}\text{K}^{-1}$, respectively, and the corresponding temperature is 650 K and 1000 K. The room-temperature κ is $19.94 \text{ Wm}^{-1}\text{K}^{-1}$ and $45.98 \text{ Wm}^{-1}\text{K}^{-1}$, respectively. These results are useful for the thermal management of ZrTe-based electronics devices.

IV. CONCLUSION

The elastic properties and phonon transport of the isostructural topological semimetal MoP has been investigated by the same method²³. It is found that the bulk modulus, shear modulus, Young's modulus of ZrTe are smaller than those of MoP, which means that ZrTe produces easily deformation by applied external force. The lattice thermal conductivity of ZrTe ($17.56 \text{ Wm}^{-1}\text{K}^{-1}$) along a(b) direction is very close to that of MoP ($18.41 \text{ Wm}^{-1}\text{K}^{-1}$), while the lattice thermal conductivity of ZrTe ($43.08 \text{ Wm}^{-1}\text{K}^{-1}$) along c direction is larger than that of MoP ($34.71 \text{ Wm}^{-1}\text{K}^{-1}$). It is noted that the average lattice thermal conductivity ($\kappa_L(av) = (\kappa_L(aa) + \kappa_L(bb) + \kappa_L(cc))/3$) of ZrTe is slightly higher than that of MoP. This is because that ZrTe has larger phonon lifetimes and smaller Grüneisen parameters than MoP, which gives rise to higher lattice thermal conductivity for ZrTe than MoP. Phonon transport of another classic topological semimetal TaAs has been investigated²⁰. Any of ZrTe, MoP and TaAs shows obvi-

ously anisotropic lattice thermal conductivity along a(b) and c directions. However, for TaAs, the lattice thermal conductivity along a(b) direction is larger than one along c direction, but the lattice thermal conductivity of ZrTe or MoP along a(b) direction is smaller than that along c direction.

In summary, the elastic and transport properties of ZrTe are performed by the first-principles calculations and semiclassical Boltzmann transport theory. The elastic tensor components C_{ij} for ZrTe are presented, which confirm the mechanical stability of the structure. The bulk modulus, shear modulus, Young's modulus and Poisson's ratio are also attained by calculated C_{ij} . The electronic transport coefficients are also calculated within CSTA Boltzmann theory. For pristine ZrTe, the Seebeck coefficient, electrical resistivity and electronic thermal conductivity will be of use for comparison with future experimental measurements. The lattice thermal conductivity of ZrTe shows an obvious anisotropy along the a(b) and c crystal axis. It is found that isotope scattering has

observable effect on the lattice thermal conductivity, and phonons with MFP larger than $0.60 \mu\text{m}$ have little contribution to the total lattice thermal conductivity. The higher lattice thermal conductivity of ZrTe than MoP can be explained by larger phonon lifetimes and smaller Grüneisen parameters. The total thermal conductivity is also attained for pristine ZrTe. Our works shed light on elastic and transport properties of ZrTe, and will motivate farther experimental studies of elastic and transport properties of topological semimetals ZrTe.

ACKNOWLEDGMENTS

This work is supported by the National Natural Science Foundation of China (Grant No.11404391). We are grateful to the Advanced Analysis and Computation Center of CUMT for the award of CPU hours to accomplish this work.

-
- ¹ R. M. Lutchyn, J. D. Sau and S. D. Sarma, *Phys. Rev. Lett.* **105**, 077001 (2010).
- ² B. Q. Lv, Z. L. Feng, Q. N. Xu et al., *Nature* **546**, 627 (2017).
- ³ C. Fang, H. M. Weng, X. Dai and Z. Fang, *Chinese Phys. B* **25**, 117106 (2016).
- ⁴ H. J. Zhang, C. X. Liu, X. L. Qi, X. Dai, Z. Fang and S. C. Zhang, *Nat. Phys.* **5**, 438 (2009).
- ⁵ X. L. Qi and S. C. Zhang, *Rev. Mod. Phys.* **83**, 1057 (2011).
- ⁶ M. Z. Hasan and C. L. Kane, *Rev. Mod. Phys.* **82**, 3045 (2010).
- ⁷ B. Q. Lv, H. M. Weng, B. B. Fu, X. P. Wang, H. Miao, J. Ma, P. Richard, X. C. Huang, L. X. Zhao, G. F. Chen, Z. Fang, X. Dai, T. Qian, and H. Ding, *Phys. Rev. X* **5**, 031013 (2015).
- ⁸ L. X. Yang, Z. K. Liu and Y. Sun et al., *Nat. Phys.* **11**, 728 (2015).
- ⁹ L. M. Schoop, M. N. Ali, C. Straßer, A. Topp, A. Varykhalov, D. Marchenko, V. Duppel, S. S. P. Parkin, B. V. Lotsch, and C. R. Ast, *Nat. Commun.* **7**, 11696 (2016).
- ¹⁰ Z. J. Wang, Y. Sun, X. Q. Chen, C. Franchini, G. Xu, H. M. Weng, X. Dai and Z. Fang, *Phys. Rev. B* **85**, 195320 (2012).
- ¹¹ Z. K. Liu, B. Zhou and Y. Zhang et al., *Science* **343**, 864 (2014).
- ¹² B. Bradlyn, J. Cano, Z. Wang, M. G. Vergniory, C. Felser, R. J. Cava and B. A. Bernevig, *Science* **353**, aaf5037 (2016).
- ¹³ H. Weng, C. Fang, Z. Fang and X. Dai, *Phys. Rev. B* **94**, 165201 (2016).
- ¹⁴ Z. M. Zhu, G. W. Winkler, Q. S. Wu, J. Li and A. A. Soluyanov, *Phys. Rev. X* **6**, 031003 (2016).
- ¹⁵ G. W. Winkler, Q. S. Wu, M. Troyer, P. Krogstrup and A. A. Soluyanov, *PRL* **117**, 076403 (2016).
- ¹⁶ C. Shekhar, Y. Sun, N. Kumar et al. arXiv:1703.03736 (2017).
- ¹⁷ J. B. He, D. Chen, W. L. Zhu, S. Zhang, L. X. Zhao, Z. A. Ren and G. F. Chen, *Phys. Rev. B* **95**, 195165 (2017).
- ¹⁸ J. Z. Ma, J. B. He, Y. F. Xu et al., arXiv:1706.02664 (2017).
- ¹⁹ W. L. Zhu, J. B. He, S. Zhang, D. Chen, L. Shan, Z. A. Ren and G. F. Chen, arXiv:1707.00942 (2017).
- ²⁰ T. Ouyang, H. P. Xiao, C. Tang, M. Hu and J. X. Zhong, *Phys. Chem. Chem. Phys.* **18**, 16709 (2016).
- ²¹ B. Peng, H. Zhang, H. Z. Shao, H. L. Lu, D. W. Zhang and H. Y. Zhua, *Nano Energy* **30**, 225 (2016).
- ²² J. Buckeridge, D. Jevdokimovs, C. R. A. Catlow and A. A. Sokol, *Phys. Rev. B* **93**, 125205 (2016).
- ²³ S. D. Guo, arXiv:1707.00088 (2017).
- ²⁴ P. Hohenberg and W. Kohn, *Phys. Rev.* **136**, B864 (1964); W. Kohn and L. J. Sham, *Phys. Rev.* **140**, A1133 (1965).
- ²⁵ J. P. Perdew, K. Burke and M. Ernzerhof, *Phys. Rev. Lett.* **77**, 3865 (1996).
- ²⁶ P. Blaha, K. Schwarz, G. K. H. Madsen, D. Kvasnicka and J. Luitz, WIEN2k, an Augmented Plane Wave + Local Orbitals Program for Calculating Crystal Properties (Karlheinz Schwarz Technische Universität Wien, Austria) 2001, ISBN 3-9501031-1-2
- ²⁷ A. H. MacDonald, W. E. Pickett and D. D. Koelling, *J. Phys. C* **13**, 2675 (1980).
- ²⁸ D. J. Singh and L. Nordstrom, *Plane Waves, Pseudopotentials and the LAPW Method*, 2nd Edition (Springer, New York, 2006).
- ²⁹ J. Kunes, P. Novak, R. Schmid, P. Blaha and K. Schwarz, *Phys. Rev. B* **64**, 153102 (2001).
- ³⁰ D. D. Koelling, B. N. Harmon, *J. Phys. C Solid State Phys.* **10**, 3107 (1977).
- ³¹ G. K. H. Madsen and D. J. Singh, *Comput. Phys. Commun.* **175**, 67 (2006).
- ³² G. Kresse, *J. Non-Cryst. Solids* **193**, 222 (1995).
- ³³ G. Kresse and J. Furthmüller, *Comput. Mater. Sci.* **6**, **15** (1996).
- ³⁴ J. P. Perdew, K. Burke and M. Ernzerhof, *Phys. Rev. Lett.* **77**, 3865 (1996).

- ³⁵ G. Kresse and D. Joubert, *Phys. Rev. B* **59**, 1758 (1999).
- ³⁶ A. Togo, L. Chaput and I. Tanaka, *Phys. Rev. B* **91**, 094306 (2015).
- ³⁷ A. Togo, F. Oba, and I. Tanaka, *Phys. Rev. B* **78**, 134106 (2008).
- ³⁸ The experimental lattice constants are attained from the Inorganic Crystal Structure Database (ICSD).
- ³⁹ H. M. Ledbetter, *J. Phys. Chem. Ref. Data* **6**, 1181 (1977).
- ⁴⁰ Z. J. Wu, E. J. Zhao, H. P. Xiang, X. F. Hao, X. J. Liu and J. Meng, *Phys. Rev. B* **76**, 054115 (2007).
- ⁴¹ B. Salmankurt and S. Duman, *Philosophical Magazine*, **97**, 175 (2017).
- ⁴² T. J. Scheidemantel, C. Ambrosch-Draxl, T. Thonhauser, J. V. Badding and J. O. Sofo, *Phys. Rev. B* **68**, 125210 (2003).
- ⁴³ G. K. H. Madsen, *J. Am. Chem. Soc.* **128**, 12140 (2006).
- ⁴⁴ X. Gao, K. Uehara, D. Klug, S. Patchkovskii, J. Tse and T. Tritt, *Phys. Rev. B* **72**, 125202 (2005).
- ⁴⁵ J. Yang, L. Xi, W. Qiu, L. Wu, X. Shi, L. Chen, J. Yang, W. Zhang, C. Uher and D.J. Singh, *npj Comput. Mater.* **2**, 15015 (2016).
- ⁴⁶ S. Ullah, J. X. Li, R. H. Li, Q. Xie, H. Ma, D. Z. Li, Y. Y. Li and X. Q. Chen, arXiv:1706.06876 (2017).
- ⁴⁷ W. Kim, *J. Mater. Chem. C* **3**, 10336 (2015).
- ⁴⁸ S. I. Tamura, *Phys. Rev. B*, **27**, 858 (1983).